# Motorcycle Tire Modeling for the Study of Tire–Rim Interaction

Federico Ballo[a], Massimiliano Gobbi[a][1], Gianpiero Mastinu[a], Giorgio Previati[a]

[a]Department of Mechanical Engineering, Politecnico di Milano, Via La Masa, 1, Milan 20158, Italy

[1]Corresponding author: massimiliano.gobbi@polimi.it

---

## Abstract

For the lightweight design of the wheel rim of motorcycles, the knowledge of the way in which contact forces are transmitted by the tire is of crucial importance. In this paper, an analytical model of the tire is developed and explicit formulae giving the distribution of the radial and axial forces acting on the wheel rim for a given vertical load are derived. The analytical model is validated by means of a finite element method (FEM) model and experimental tests. The proposed analytical model is able to predict the radial deflection of both a front and a rear tire for a racing motorbike with very good accuracy over a wide range of inflating pressures and vertical loads. The force distributions are in very good agreement with the results of the FEM model. Experimental tests show that the force distribution at the interface between the tire and rim can be used to predict the stress distribution in the rim with a good accuracy.

## 1 Introduction

Understanding how contact forces are transferred to the rim is a crucial factor for a lightweight design of vehicle wheels. The numerical models most widely used for the design of vehicle wheels include the loads acting on the wheel rim in a simplified way [1–5]. The knowledge of the actual distribution of the reaction forces applied by the tire to the rim should be known in order to design a lighter and more structurally efficient component. The effect of camber angle is predominant in motorcycles, compared to cars. In motorcycles, the forces acting along the radial direction (and parallel to the wheel plane) are significantly higher than forces acting in a pure lateral direction.

To the best of our knowledge, few papers on the structural behavior of motorcycle tires can be found in the literature. Referring to motorcycle tire dynamic behavior, Lot [6] developed a model for contact forces estimation and employed it for real time simulations of the bike dynamics. An interesting work on motorcycle tire properties and issues related to experimental measurements can be found in Ref. [7]. Pacejka's magic formula was employed in Ref. [8] for characterizing tires of a light motorcycle. All the mentioned references are focused on the computation of tire/road contact forces, but in no case, information about the tire/rim interaction is given.

Several simplified structural models for car vehicle tires are described in some papers. The rigid ring SWIFT tire model was employed in Refs. [9] and [10] for describing tire vertical and longitudinal dynamics when simulating vehicle ABS braking.

The studies on lateral and longitudinal tire dynamics through simplified structural models were proposed in Refs. [11–13] for evaluating the transient response of ground vehicles.

A flexible ring tire model was employed by Kim et al. [14] for studies on vehicle handling and ride comfort for low frequency ranges. The flexible ring scheme is based on a deformable ring on an elastic foundation that represents the tire sidewalls. The same model was used for investigating tire natural frequencies and noise emissions of moving vehicles [15,16].

Structural models for the study of tire high frequency response are discussed in Refs. [17–19].

Analytical expressions of vertical stiffness of several vehicle tires can be found in Refs. [20] and [21].

A large number of tire models are based on finite-element methods. Finite element based tire models can reach a high level of accuracy since the detailed tire structure and all its components can be modeled [22,23]. FEM models are very informative but, in general, at a high computational cost. Moreover, the proper development of a FEM model requires the knowledge of a large number of parameters related to the tire structure and material properties [24–33]. Such an effort could be not always sustainable by wheel manufacturers, especially because it is generally hard to obtain tire structural and geometrical properties. In these cases, a simpler, even if relatively less accurate, model that requires a very limited number of parameters can be effectively employed for the design of the rim. In fact, a simplified model able to predict the distribution of the reaction forces on the rim at a low computational cost and requiring the knowledge of few tire parameters can be a valuable tool. A simple analytical model of a motorbike tire was developed by Ballo et al. [34], which is able to compute the interaction forces between the tire and rim. In this paper, significant improvements of the model are discussed and presented.

This paper is organized as follows: In Sec. 2, the mathematical formulation of the analytical model is presented along with the computed deformed shapes and reaction loads for a front and rear tire subject to a vertical load. Then, a detailed FEM model of the rear tire is developed to validate the analytical model. Experimental tests on a front and rear tire are described in Sec. 4, and the experimental validation of the analytical and FEM models is

presented. An improved nonlinear tire model is presented in Sec. 5. Section 6 shows the actual capabilities of the developed model through direct comparison with experimental measurements performed on an actual motorcycle wheel.

## 2  Tire Analytical Model

The analytical model presented in this section is based on the model derived by Kim et al. [14]. The model was derived in order to compute pressure and shear stress/strain distributions in the contact patch of a car tire under a vertical load.

In the following, the model reported in Ref. [14] is adapted to a motorbike tire. The reaction forces acting on the wheel rim when a vertical load is applied are explicitly computed.

The model is depicted in Fig. 1 and consists of an external deformable curved beam connected to the wheel rim (considered rigid and represented in Fig. 1 by the internal ring) by means of linear springs.

The linear springs are actually modeled as a distributed spring (stiffness per unit of length). The wheel rim is assumed as a rigid body; therefore, the internal ring is fixed to the ground.

The above-described tire model, when loaded by a vertical load, is symmetric with respect to a vertical axis passing through the center of the tire.

The curved beam accounts for the bending stiffness of the tread, described by the parameter $EJ$. $k$ (N/mm$^2$) is the residual radial stiffness per unit of length of the tire carcass. In the radial stiffness $k$, the stiffening effect of the inflation pressure is also considered. $EJ$ and $k$ represent the physical properties of the tire and, therefore, their numerical values have to be identified for the actual tire under consideration.

The identification of the parameters can be performed experimentally as shown in Sec. 4.2.

Let us consider a portion $ds$ defined by an infinitesimal angle $d\phi$ of a general curved beam (Fig. 2).

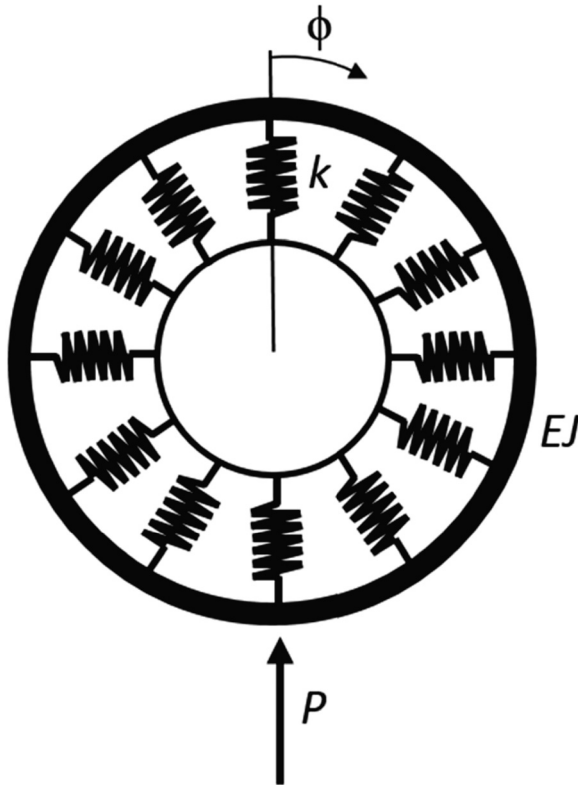A positive displacement $u$ in the radial direction $n$ moves point $Q$ to point $Q_d$.



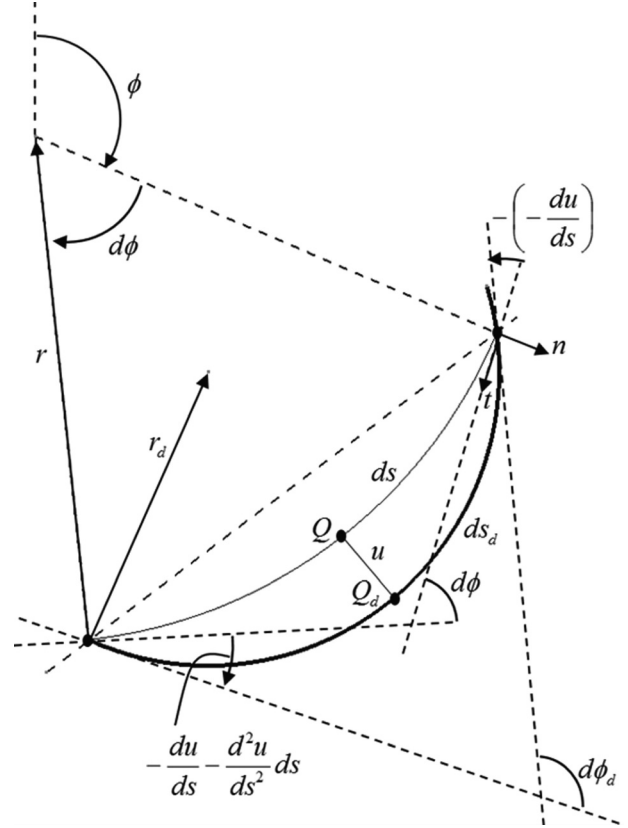**Fig. 1 Simplified analytical tire model for radial deflection [14]**



**Fig. 2   Portion *ds* of a general curved beam**

If $u \ll r$, the length $ds_d$ of the deformed arch can be expressed as ($r < 0$ since it points toward the center)

$$ds_d = ds - \frac{u}{r}ds \qquad (1)$$

The curvature of the undeformed beam reads

$$\frac{1}{r} = -\frac{d\phi}{ds} \qquad (2)$$

While the curvature in the deformed configuration can be expressed as

$$\frac{1}{r_d} = -\frac{d\phi_d}{ds_d} = -\frac{d\phi - \frac{d^2u}{ds^2}ds}{\left(1 - \frac{u}{r}\right)ds} = -\frac{d\phi - \frac{d^2u}{ds^2}ds\left(1 + \frac{u}{r}\right)}{\left(1 - \frac{u}{r}\right)ds\left(1 + \frac{u}{r}\right)}$$

$$\approx \frac{1}{r} + \frac{u}{r^2} + \frac{d^2u}{ds^2} \qquad (3)$$

where $d\phi_d$ is obtained by considering the deformed beam of Fig. 2 and reads

$$d\phi_d = d\phi + \frac{du}{ds} + \left(-\frac{du}{ds} - \frac{d^2u}{ds^2}ds\right) = d\phi - \frac{d^2u}{ds^2}ds \qquad (4)$$

The change in the curvature is proportional to the bending moment $M$

$$\frac{1}{r_d} - \frac{1}{r} = -\frac{M}{EJ} \rightarrow \frac{d^2u}{ds^2} + \frac{u}{r^2} = \frac{1}{r^2}\left(\frac{d^2u}{d\phi^2} + u\right) = -\frac{M}{EJ} \qquad (5)$$

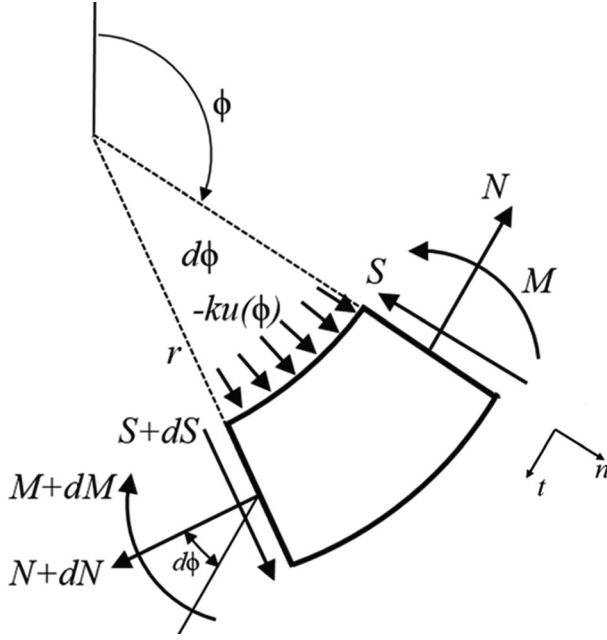The portion $ds$ of the curved beam is subjected to internal and external forces as shown in Fig. 3.

$$\frac{d^5 u}{d\phi^5} + 2\frac{d^3 u}{d\phi^3} + \left(1 + \frac{kr^4}{EJ}\right)\frac{du}{d\phi} = 0 \tag{13}$$

Equation (13) is a homogeneous linear differential equation in the unknown displacement $u(\phi)$. The solution of this equation provides the radial displacement $u(\phi)$ of the tire when subjected to a concentrated force. The solution of Eq. (13) has the general form

$$u(\phi) = U_0 e^{m\phi} \tag{14}$$

The characteristic equation reads

$$(m^5 + 2m^3 + \delta^2 m)U_0 e^{m\phi} = 0 \tag{15}$$

with $\delta = \sqrt{(kr^4/EJ) + 1}$.

Equation (15) has five distinct roots

$$\begin{cases} m_1 = 0 \\ m_{2,3,4,5} = \pm\alpha\pm i\beta \end{cases} \tag{16}$$

with

$$\begin{cases} \alpha = \sqrt{\dfrac{\delta - 1}{2}} \\ \beta = \sqrt{\dfrac{\delta + 1}{2}} \end{cases} \tag{17}$$

The solution therefore reads

$$u(\phi) = U_1 e^{m_1\phi} + U_2 e^{m_2\phi} + U_3 e^{m_3\phi} + U_4 e^{m_4\phi} + U_5 e^{m_5\phi} \tag{18}$$

which, after rearranging the terms and grouping some constants, simplifies to

$$u(\phi) = C_0 + \cos(\beta\phi)[C_1\cosh(\alpha\phi) + C_2\sinh(\alpha\phi)]$$
$$+ \sin(\beta\phi)[C_3\cosh(\alpha\phi) + C_4\sinh(\alpha\phi)] \tag{19}$$

The five constants can be computed by applying the following boundary conditions:

$$\begin{cases} \left.\dfrac{du}{d\phi}\right|_{\phi=0} = 0 \\ \left.\dfrac{du}{d\phi}\right|_{\phi=\pi} = 0 \\ S_{\phi=0} = 0 \\ S_{\phi=\pi} = -\dfrac{P}{2} \\ \dfrac{r}{EJ}\displaystyle\int_0^\pi M d\phi = \dfrac{1}{EJr}\displaystyle\int_0^\pi \left(\dfrac{d^2 u}{d\phi^2} + u\right)d\phi = 0 \end{cases} \tag{20}$$

where the first two conditions account for the symmetry of the solution with respect to the vertical axis. The third and fourth conditions express the shear force at $\phi = 0$ and $\phi = \pi$. The last condition, when the first two conditions hold, states the conservation of the length of the curved beam representing the tire tread. Equation (20) shows that the effect of a concentrated force can be introduced only as boundary condition. External loads can be introduced only under the form of continuously distributed loads acting on the whole curved beam as it will be shown in Sec. 5.

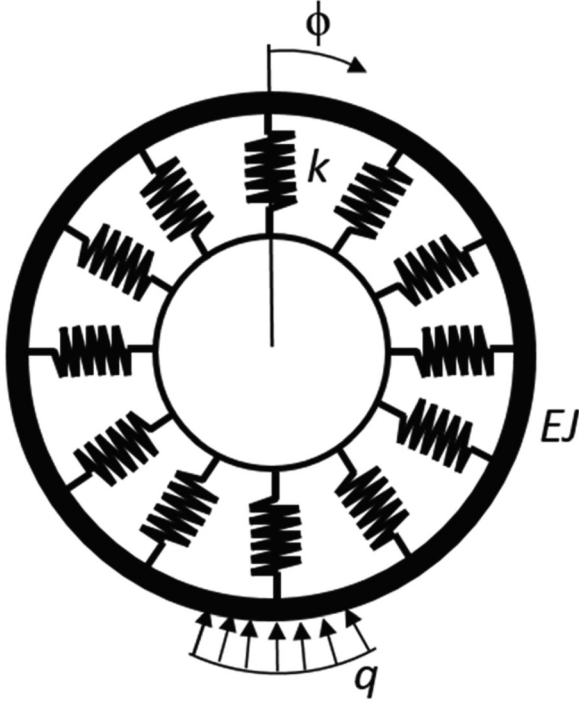The solution of system (20) provides the five constants of Eq. (19)

---



**Fig. 3   Free-body diagram of a portion *ds* of the curved beam**

The equilibrium in the tangential direction $t$ reads

$$-N + (N + dN)\cos(d\phi) + (S + dS)\sin(d\phi) = 0 \tag{6}$$

which, by considering $\cos(d\phi) \approx 1$ and $\sin(d\phi) \approx d\phi$ and neglecting higher order terms, gives

$$dN = -S d\phi \tag{7}$$

From the equilibrium of rotation, we obtain

$$M - (M + dM) + (S + dS)\cos(d\phi)\cdot rd\phi$$
$$- (N + dN)\sin(d\phi)\cdot rd\phi = 0 \tag{8}$$

which, by remembering that $\cos(d\phi) \approx 1$ and $\sin(d\phi) \approx d\phi$ and neglecting higher order terms, can be rewritten as

$$S = \frac{1}{r}\frac{dM}{d\phi} \tag{9}$$

Finally, the equilibrium in the radial direction $n$ reads

$$S - (S + dS) + (N + dN)d\phi + kur d\phi = 0 \rightarrow \frac{dS}{d\phi} = N + kru(\phi) \tag{10}$$

By substituting Eq. (9) in Eq. (10), the following relation is obtained:

$$\frac{1}{r}\frac{d^2 M}{d\phi^2} = N + kru(\phi) \tag{11}$$

By deriving Eq. (11) with respect to $\phi$ and remembering Eqs. (7) and (9), we obtain

$$\frac{1}{r}\frac{d^3 M}{d\phi^3} = -\frac{1}{r}\frac{dM}{d\phi} + kr\frac{du}{d\phi} \tag{12}$$

From Eq. (5), we know the relation between $u$ and $M$ and therefore

**Fig. 4  Tire analytical model with a distributed load**

$$\begin{cases} C_0 = \dfrac{\mathrm{P}r^3}{2\pi EJ\delta^2} \\[2mm] C_1 = \dfrac{\mathrm{P}r^3\big[\alpha\cosh(\alpha\pi)\sin(\beta\pi) + \beta\cos(\beta\pi)\sinh(\alpha\pi)\big]}{2EJ\alpha\beta(\alpha^2 + \beta^2)\big[\cos(2\pi\beta) - \cosh(2\pi\alpha)\big]} \\[2mm] C_2 = 0 \\[2mm] C_3 = 0 \\[2mm] C_4 = \dfrac{\mathrm{P}r^3\big[\beta\cosh(\alpha\pi)\sin(\beta\pi) - \alpha\cos(\beta\pi)\sinh(\alpha\pi)\big]}{2EJ\alpha\beta(\alpha^2 + \beta^2)\big[\cos(2\pi\beta) - \cosh(2\pi\alpha)\big]} \end{cases} \quad (21)$$

The described model is derived considering a concentrated vertical force applied to the tire. In an actual tire, the vertical force is applied by means of a pressure distribution in the contact patch (Fig. 4).

Now if the uniform pressure distribution of Fig. 4 is considered, the depicted loading condition can be approximated by a superposition of pointwise loads. In fact by discretizing the angular sector of the contact patch with $N$ increments, $\Delta\phi_i$ the tire radial deflection can be expressed as

$$u(\phi) = \frac{P}{N}\sum_{i=1}^{N}\bar{u}(\phi, \phi_i) \quad (22)$$

where $\bar{u}(\phi, \phi_i)$ is the radial deformation of the tire subjected to a concentrated unit load at $\phi_i$.

Radial forces per unit length acting on the wheel rim can then be computed as

$$dT_{\mathrm{rad},q} = ku(\phi)\frac{r}{r_{\mathrm{rim}}} \quad (23)$$

where the scaling factor $r/r_{\mathrm{rim}}$ accounts for the different values of the radius of the tire and the rim.

The forces in the lateral direction (i.e., the direction of wheel rotation axis) can be approximated according to the scheme of Fig. 5, where the half cross section of the tire is depicted.

The lateral force on the wheel rim reads

$$dT_{ax} \approx \frac{ph(\phi)}{2} = \frac{p(h_0 + u(\phi))}{2} \quad (24)$$

with the approximation $dT_0 = dT_{ax}$ [1].

The model of Fig. 4 is not able to compute the contribution of inflation pressure on the reaction forces. For this purpose, the simplified scheme of Fig. 6 is considered [21].

The tread is considered as a rigid ring with rectangular cross section. The sidewall is modeled as a membrane element [11,20,21], the tension force $s$ reads

$$s = \frac{ph_s}{2\sin\left(\dfrac{\theta}{2}\right)} \quad (25)$$

The total forces acting on the rim are given by the sum of all the contributions and read

$$\begin{cases} dT_{\mathrm{rad}} = \dfrac{dT_{\mathrm{rad},q}}{2} + dT_{\mathrm{rad},p} \\[3mm] dT_{ax} \end{cases} \quad (26)$$

where $dT_{\mathrm{rad},p}$ is the projection of $s$ in the radial direction. In Table 1, the parameters pertaining to a front and a rear tire of a race motorcycle are reported (see Sec. 4 for the experimental identification of the structural parameters $k$ and $EJ$).

The residual stiffness $k$ is defined as the sum of the contribution of the structural stiffness of the tire sidewalls and the stiffening effect of the inflation pressure. In Fig. 7, the dependence of the residual stiffness to the inflation pressure is shown. It can be observed that the residual stiffness increases linearly with the inflation pressure. The residual stiffness at inflation pressure equal to zero represents the structural stiffness of the tire sidewalls.
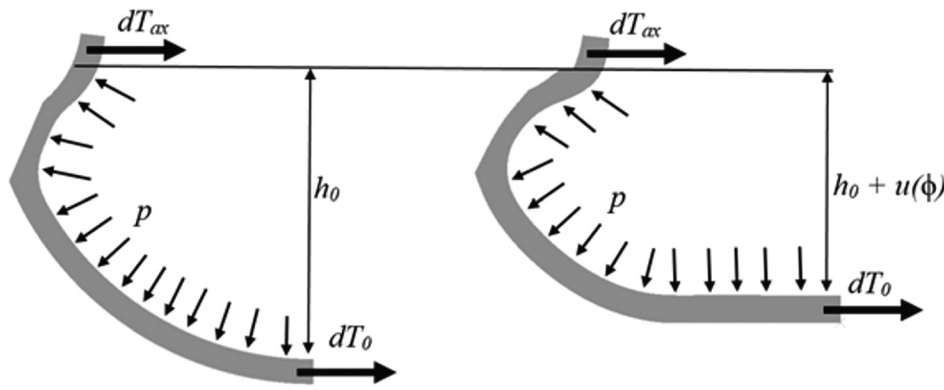


**Fig. 5  Tire reaction forces in lateral direction: undeformed tire (left) and deformed tire (right)**
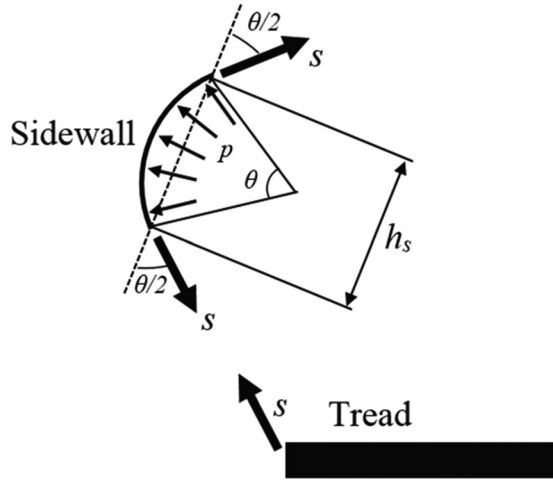
**Fig. 6 Tire radial forces when only an inflation pressure is applied**

**Table 1 Analytical model parameters for front and rear tires**

|  | Front tire (120/70 R420) | Rear tire (200/60 R17) |
|---|---|---|
| $r$ (mm) | 290 | 320 |
| $h_0$ (mm) | 80 | 105 |
| $h_s$ (mm) | 35 | 35 |
| $\theta$ (deg) | 55 | 55 |
| $EJ$ (N/mm$^2$) | $18 \times 10^6$ | $9 \times 10^6$ |
| $k$ (N/mm$^2$)[a] | $0.241\,p + 0.175$ | $0.187\,p + 0.0675$ |

[a] The residual stiffness is expressed as a function of the tire inflation pressure $p$ (bar).

The radial displacements of the front and rear tire (inflated at their nominal pressure) when subjected to a total vertical force of 2500 N are reported in Figs. 8 and 9.

## 3 Tire FEM Model

In this section, a FEM model of the rear tire of a race motorbike (size 200/60R17) considered in Table 1 is described.

The FEM model takes into account the actual shape and internal structure of the tire. This model, being more detailed, can be used to validate the reaction forces computed by the analytical model developed in Sec. 2. The experimental validation of the FEM model in vertical and lateral directions is shown in Sec. 4.

The geometry of the tire actual cross section and the identification of the tire structural components are obtained throughout optical measures performed by the wheel manufacturer. The obtained shape is discretized by finite elements. The actual structure of the tire is modeled, i.e., the beads, the 0 deg (circumferential) steel ply and the 90 deg (radial) ply are considered in the model. Figure 10 shows the FEM model of the tire, and the structural components are highlighted.

The tire beads and the rubber structure are modeled by the homogeneous material. Due to the lack of information on the actual compounds of the tire structure, an approximation is made by modeling the rubber structure with a single material. An incompressible Neo-Hookean model is employed for describing the rubber material property [35]. Steel material is employed for modeling the tire beads. The two plies are modeled by rebar layers embedded in the rubber solid elements as shown in Fig. 10. The 0 deg ply is embedded in the tire tread and is made by equally spaced steel wires modeled by rebar elements. The 90 deg ply reinforcement is embedded in the entire rubber carcass and is made by elastic wires. Material and geometric parameters are identified basing on the experimental tests described in Sec. 4. The identified values are consistent with the ones that can be found in the literature [24,26,28,36,37] and are summarized in Tables 2 and 3.

The numerical simulation is divided in two steps [24–29,38]:

- two-dimensional axisymmetric FEM model of the inflated tire and
- three-dimensional model generation by revolving the axisymmetric model and application of radial and lateral loads.

In the first step, a 2D nonlinear axisymmetric model of the tire cross section subjected to inflation pressure is considered. The inflation pressure is applied as follower distributed pressure forces acting at the inner side of the tire surface. Linear axisymmetric quad elements are employed for the analysis, the tire is fixed at the wheel interface (see Fig. 11).

In the second step of the analysis, the inflated section of the tire obtained from the first step of the analysis is revolved to generate a 3D model of the whole tire. A dense mesh of linear brick ele-ments is created near the footprint, while for the remaining tire sector a coarser mesh of 12-nodes cylindrical brick elements with trigonometrical shape functions in the circumferential direction [39] is employed in order to reduce computation time by maintaining accurate results. Twenty rows of linear brick elements are employed on a 40 deg sector across the contact patch, while for the remaining 320 deg ten rows of cylindrical brick elements are used (Fig. 12).

The road surface is modeled by a rigid plane (Fig. 12) and a

Coulomb friction model ($\mu = 1.3$) is employed for defining the contact behavior between the tire and road surface.

Dealing with static loads, a constant friction coefficient is considered. Displacement of the rigid surface is controlled, and the vertical and lateral stiffness tests are simulated as shown in Fig. 13.
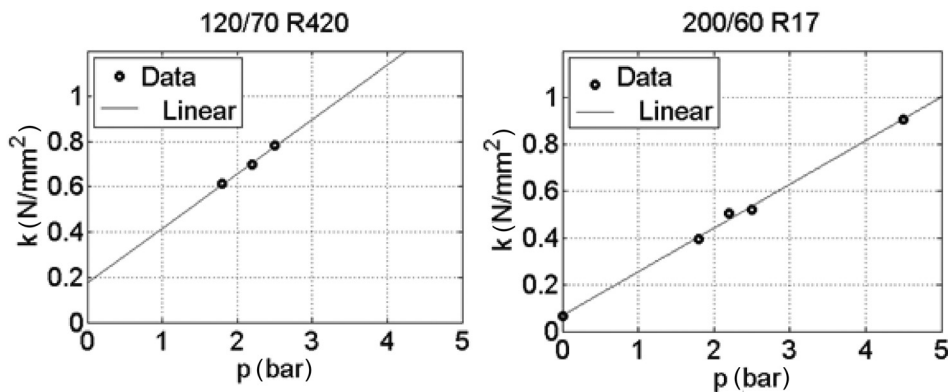


**Fig. 7 Tire residual stiffness *k* as a function of the inflation pressure: front tire (left) and rear tire (right). Dots: experimental data. Continuous line: expression of *k* from Table 1.**
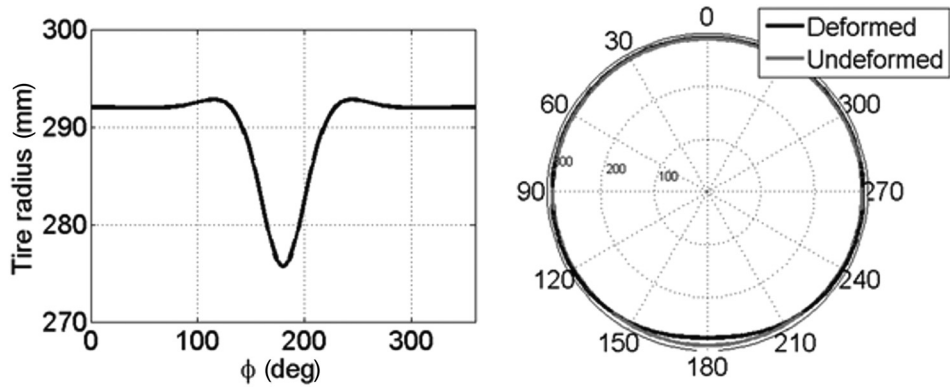
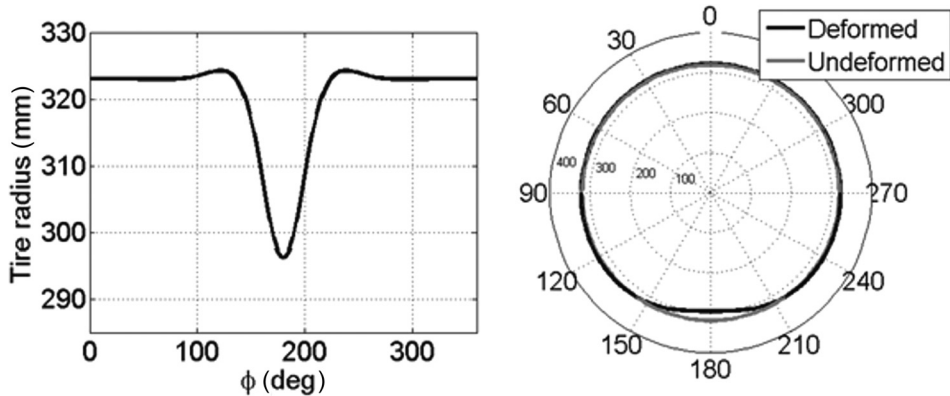**Fig. 8  Front tire radial displacement: vertical load 2500 N and inflation pressure 2.1 bar**



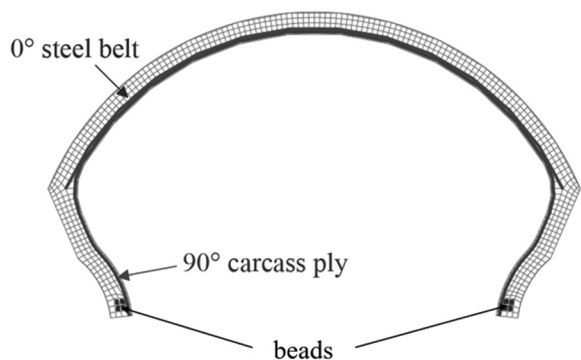**Fig. 9  Rear tire radial displacement: vertical load 2500 N and inflation pressure 1.8 bar**



**Fig. 10  Tire cross section: FEM model**

**Table 2  Material properties of the tire structure—200/60 R17 motorcycle race tire**

|  | Material type | Value |
| --- | --- | --- |
| Bead | Isotropic | $E = 210$ GPa, $\nu = 0.3$ |
| 0 deg ply | Isotropic | $E = 210$ GPa, $\nu = 0.3$ |
| 90 deg ply | Isotropic | $E = 5$ GPa, $\nu = 0.4$ |
| Rubber | Incompressible Neo-Hooke | $C_{10} = 0.23$ MPa |

**Table 3  Geometric properties of reinforcements—200/60 R17 motorcycle race tire**

|  | Distance between wires (mm) | Area per wire (mm$^2$) |
| --- | --- | --- |
| 0 deg ply | 1 | 0.62 |
| 90 deg ply | 1 | 0.70 |

## 4  Experimental Tests and Model Validation

The developed analytical and FEM models of the tire are validated with the experimental results.

In this section, the experimental tests are first described. The identification of the parameters of the analytical and FEM model and the validation are then presented.

**4.1  Experimental Testing.** The radial and lateral stiffness tests on the front and rear tire are performed. The tires are mounted on a wheel and fixed to a device for applying the vertical and lateral loads as shown in Fig. 14.

The device consists of a hydraulic actuator that provides the vertical load by moving the entire system in the vertical direction. A six-axis load cell is mounted between the actuator and the tire
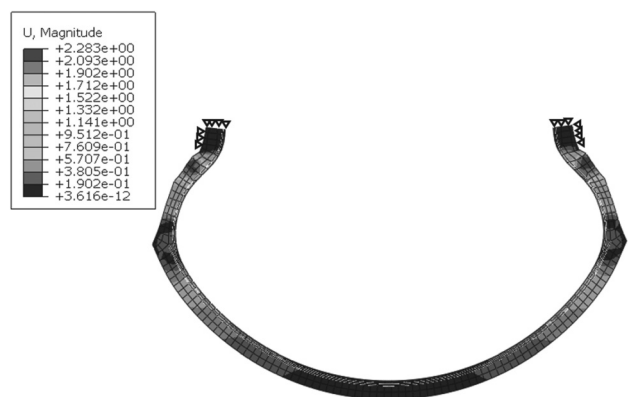


**Fig. 11  Tire cross section subjected to inflation pressure: 2D axisymmetric model**

**Fig. 12 Three-dimensional tire model for stiffness test simulation**



**Fig. 14 Test bench for tire radial and lateral stiffness measurement**

surface. The employed load cell was conceived, realized, and tested at the Politecnico di Milano, Milan, Italy. The six-axis force sensor is thoroughly described in several papers [40–42]. The sensor performances are reported in Table 4.

The six-axis load cell is mounted on a sliding platform (see Fig. 14) that allows loads to be applied in the lateral and longitudinal directions. The sliding platform is made by two thick steel plates with two linear ball bearings that allow the two degrees-of-freedom (lateral and longitudinal). Another actuator connected to the sliding platform provides the lateral force. The vertical and lateral displacements of the sliding platform are measured by means of displacement transducers.

Tire footprints are also measured. White chalk powder is scattered on the tire tread, and a black thin cardboard is placed on the pressing surface. The tire footprint left on the cardboard sheet at a given inflation pressure and vertical load is then measured.
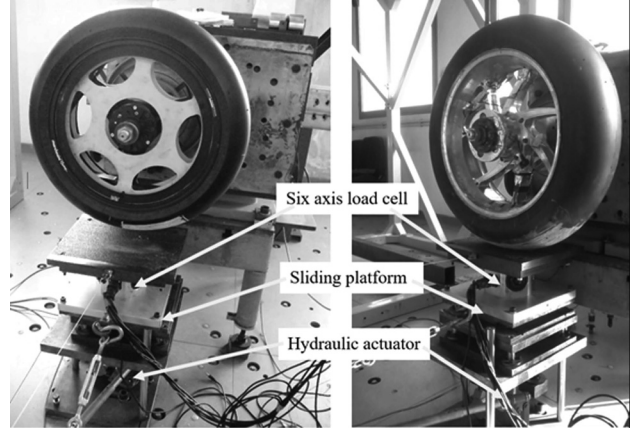
**4.2 Parameters Identification.** The structural parameters $k$ and $EJ$ of the analytical model are identified based on the measured stiffness curves.

The squared error between the experimental and the simulated vertical force is minimized

$$\min_{k,EJ}\left(\sum_{i=1}^{K}(F_{z,e}^{i}(z) - F_{z}^{i}(z))^{2}\right) \qquad (27)$$

where $F_{z,e}$ and $F_z$ are the measured and simulated vertical loads for the $K$ points considered.

The identification is conducted for several values of the inflation pressure. The results showed that $EJ$ is weakly affected by the tire pressure, and therefore, a constant value for this parameter is considered. The tire residual stiffness $k$ instead exhibits a linear trend with $p$ as shown in Fig. 7.

The same approach is followed for the FEM model. In this case, the unknown parameters are the Neo-Hooke coefficient $C_{10}$ of the rubber material, material parameters of the 90 deg ply layer, and the equivalent geometrical properties (area and distance between wires) of the two reinforcements (Table 3). Numerical values are obtained by minimizing the distance between the measured and simulated stiffness characteristics. Several inflation pressures are considered in the identification process, and the unique set of material and geometrical parameters of Tables 2 and 3 is
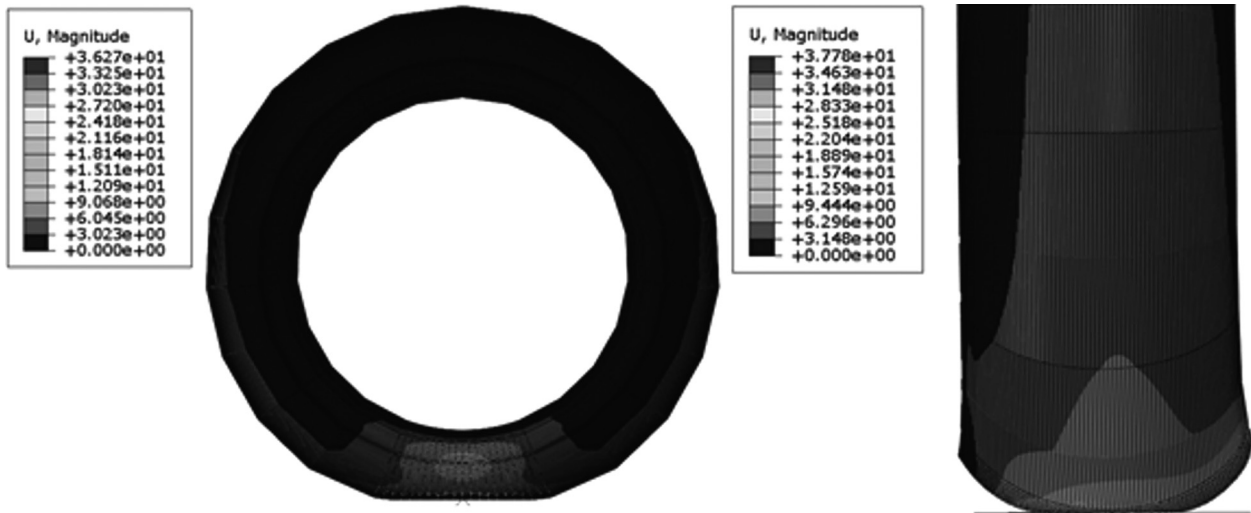


**Fig. 13 Tire radial (left) and lateral (right) stiffness test simulation**

| Maximum force | $F_x$ | 5 | kN |
|---|---|---|---|
| | $F_y$ | 10 | kN |
| | $F_z$ | 5 | kN |
| Uncertainty | 95% full scale (FS) | 0.35 | % |
| Maximum torque | $M_x$ | 0.5 | kN m |
| | $M_y$ | 0.25 | kN m |
| | $M_z$ | 0.5 | kN m |
| Uncertainty | 95% FS | 0.23 | % |
| Total mass | | 2.7 | kg |
| Bandwidth | | 350 | Hz |
| Cross-talk | | $< \pm 1\%$ | |
| Hysteresis | % FS | <0.1% FS | |

derived. The identified values are comparable with the data available in the literature (mostly related to vehicle tires) [24,26,28,36,37].

**4.3 Model Validation.** The simulations from the analytical model are compared with experiments on both the front and rear tires as shown in Figs. 15 and 16.

The rear tire FEM model is validated for radial and lateral stiffnesses (see Figs. 17 and 18).

The results show a very good agreement of both the analytical and the FEM models with the experimental data. Also, the tire

footprint is measured and compared with the output of the FEM simulation with satisfactory results as shown in Fig. 19. The difference between the measured and computed contact area is 12%.

In Figs. 20 and 21, the reaction forces acting on the rim calculated by the analytical model are compared with the ones obtained from the FEM simulations. Outside the contact patch, the radial force curves differ by about 19%. The error increases up to 35% for angles around 130 deg. For the axial force, a lower discrepancy is found.

Despite its simplicity, the analytical model proved to be effective in describing the actual interaction between the tire and rim. This simplified model could provide the designer important information on how radial forces should be applied on the wheel.

## 5   Nonlinear Tire Model

The residual stiffness $k$ depends on the tire structural characteristics and geometry. As shown in Fig. 5, when a vertical load is applied the tire cross section undergoes significant geometric variations which affect the local stiffness of the tire carcass. Therefore, a nonuniform value of the residual stiffness along the tire circumference has to be considered.

Since geometric variations of the tire cross section are related to the radial deflection, a relation between the residual stiffness $k$ and the radial displacement $u$ is introduced

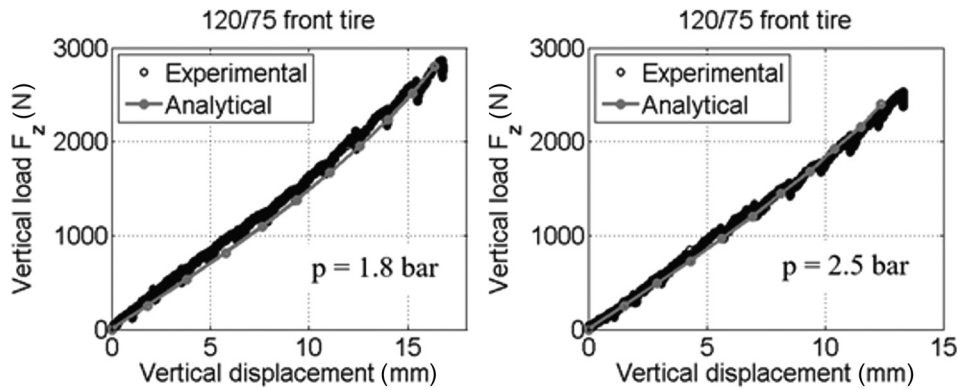$$k(u(\phi)) = a + b \cdot u(\phi) \tag{28}$$



**Fig. 15   A 120/75 R420 front tire radial stiffness for two different inflation pressures: 1.8 bar (left) and 2.5 bar (right)**
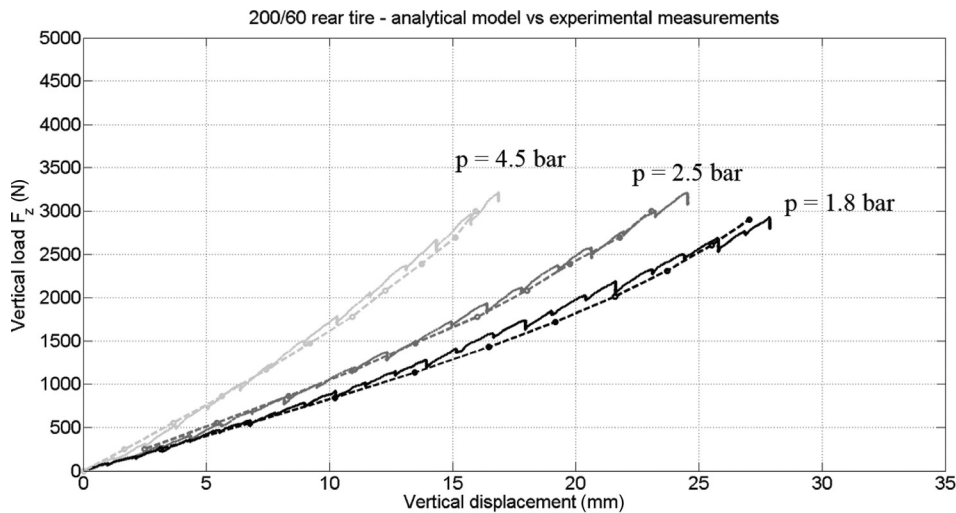


**Fig. 16   A 200/60 R17 rear tire radial stiffness for different inflation pressures: analytical model (dashed lines) and experimental measurements (dotted lines)**
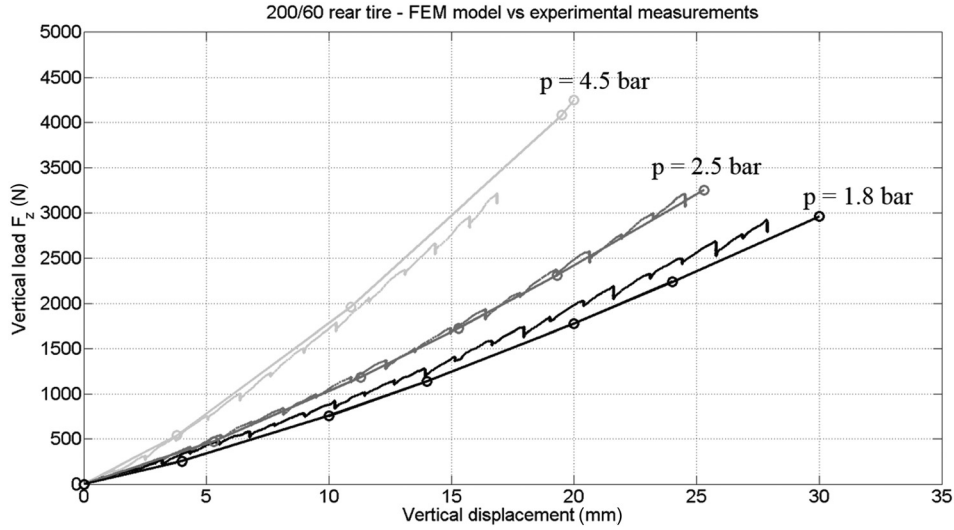
**Fig. 17** A 200/60 R17 rear tire radial stiffness for different inflation pressures: FEM model (continuous lines) and experimental measurements (dotted lines)

where the parameters $a$ and $b$ have to be identified.

In the curved beam model of Fig. 22, a generic distributed load $q(\phi)$ is added.

The distributed load $q(\phi)$ acts on the entire length of the beam and can be described by any continuous function. In this case, the uniform load $q$ is approximated with the following sigmoid function:

$$q(\phi) = A \cdot \frac{1}{1 + \exp^{(-\tau\phi + \eta)}} \qquad (29)$$

where the parameters A, $\tau$, and $\eta$ depend on the load magnitude and the distribution arch (reference values are reported in Table 5).

By applying all the passages of Sec. 2 and remembering that the derivative of $k(\phi)$ with respect to $\phi$ can be obtained through the chain rule as $(dk/d\phi) = (dk/du) \cdot (du/d\phi)$, the following relation is obtained:

$$\frac{d^5u}{d\phi^5} + 2\frac{d^3u}{d\phi^3} + \left(1 + \frac{k(u)r^4}{EJ} + \frac{r^4}{EJ}\frac{dk(u)}{du}u\right)\frac{du}{d\phi} + \frac{r^4}{EJ}\frac{dq(\phi)}{d\phi} = 0 \qquad (30)$$
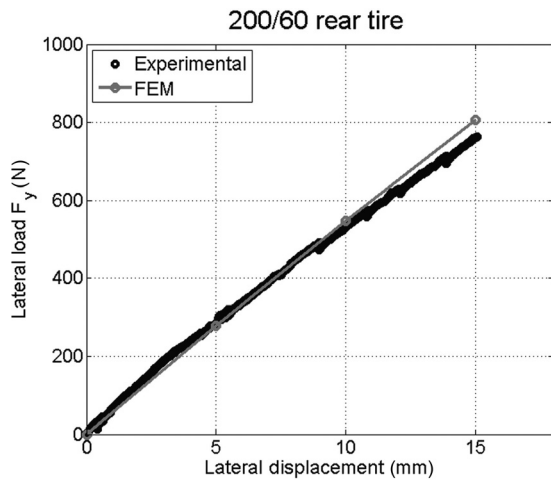
Equation (30) is now a nonlinear differential equation in the unknown displacement $u(\phi)$, and a numerical integration is required.

The five boundary conditions now read

$$\begin{cases} \left.\dfrac{du}{d\phi}\right|_{\phi=0} = 0 \\[2mm] \left.\dfrac{du}{d\phi}\right|_{\phi=\pi} = 0 \\[2mm] S_{\phi=0} = 0 \\[2mm] S_{\phi=\pi} = 0 \\[2mm] \dfrac{r}{EJ}\displaystyle\int_0^\pi Md\phi = \dfrac{1}{EJr}\displaystyle\int_0^\pi \left(\dfrac{d^2u}{d\phi^2} + u\right)d\phi = 0 \end{cases} \qquad (31)$$



**Fig. 18** A 200/60 R17 rear tire lateral stiffness for $p = 1.8$ bar: FEM model and experimental measurements
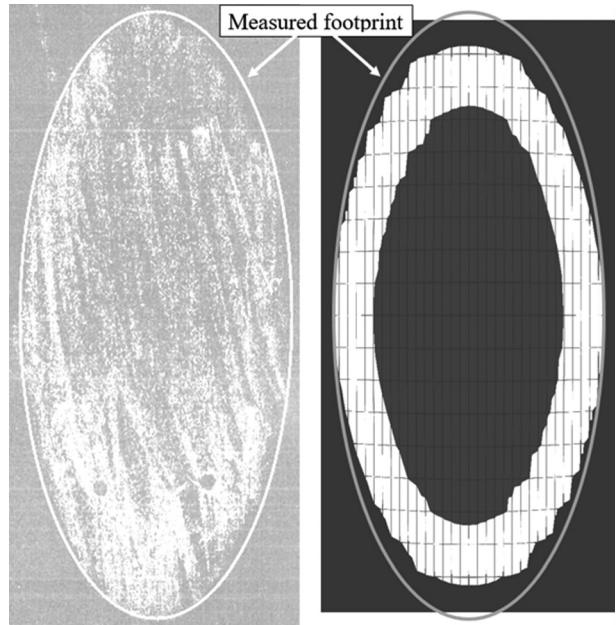


**Fig. 19** Measured and FEM-simulated footprint: vertical load 2500 N and $p = 1.8$ bar. The two pictures have the same scale.
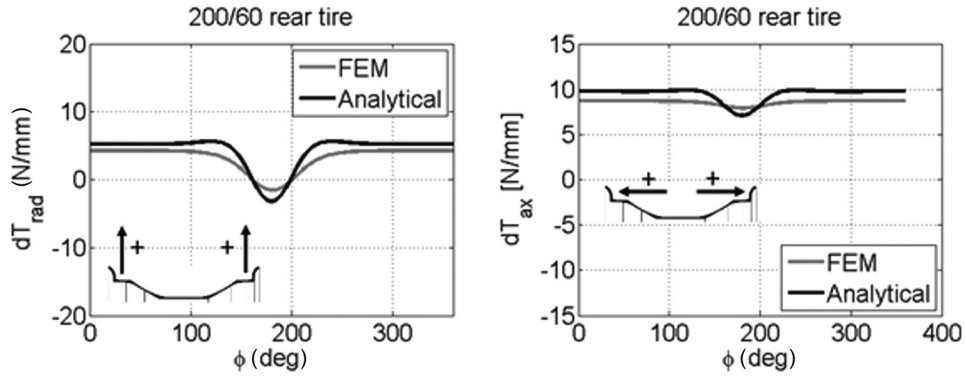
**Fig. 20   Distributed forces acting on the rim in radial (left) and axial (right) directions: 200/70 R17 rear tire, inflation pressure 1.8 bar, and vertical load 2950 N**
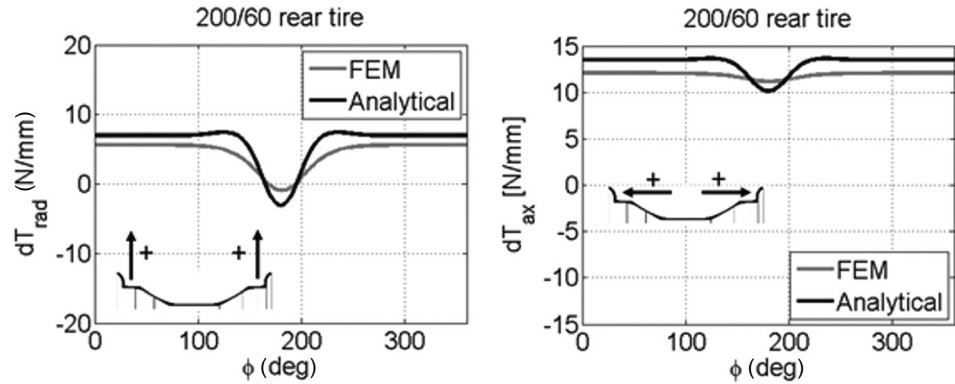


**Fig. 21   Distributed forces acting on the rim in radial (left) and axial (right) directions: 200/70 R17 rear tire, inflation pressure 2.5 bar, and vertical load 3180 N**

which are identical to Eq. (20) except for the fourth condition that now has to be equal to 0 for preserving symmetry.

The parameters $a$ and $b$ that describe the residual stiffness are identified on the basis of the experimental data. For a 200/60 R17 rear tire at an inflation pressure of 1.8 bar, the identified values are: $a = 0.375$ and $b = 0.0013$.
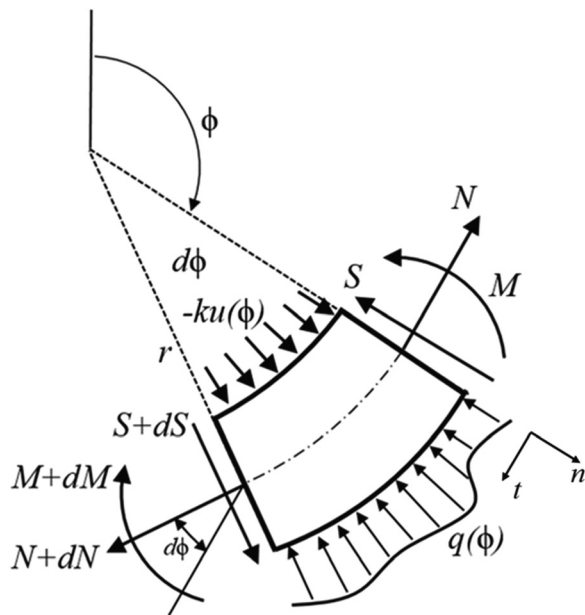


**Fig. 22   Curved beam model with a general distributed load**

Figure 23 shows the stiffness curve computed with the nonlinear model compared with the experimental results.

The radial forces acting on the wheel rim are reported in Fig. 24 and compared with the ones obtained from the linear and FEM models. The nonlinear model is closer to the FEM results especially at the center of the contact patch.

## 6   Experimental Validation of the Rim Stress Distribution

In this section, the comparison between the computed and measured deformations on an actual motorcycle wheel rim is presented. The wheel rim is instrumented by means of a set of strain gauges (SG) located on the outer rim as shown in Fig. 25.

Four 350 Ω uniaxial SG with a measuring grid of 3 mm are employed. The tire is inflated at 1.8 bar, and a vertical load of 2500 N is applied with the same procedure described in Sec. 4.1. The signals from the SG are acquired at a sampling frequency of 440 Hz.

The same test is simulated by means of a finite-element model.

The FE model of the wheel rim is shown in Fig. 26 and realized by a second-order tetrahedral mesh with average element size of 5 mm. The rim is fixed at the bearings location.

**Table 5   Parameters of the load distribution function**

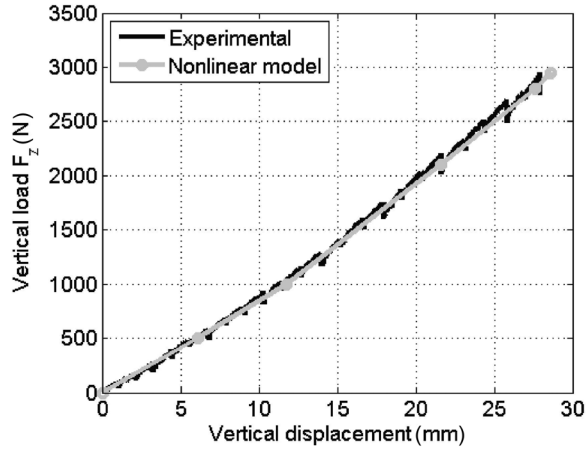| Vertical load (N) | $A$ | $\tau$ | $\eta$ |
|---|---|---|---|
| 500 | 8.29 | 100 | $97\pi$ |
| 1000 | 9.95 | 100 | $95\pi$ |
| 2100 | 10.99 | 100 | $90.5\pi$ |
| 2800 | 12.89 | 100 | $89.2\pi$ |
| 2950 | 13.10 | 100 | $88.8\pi$ |

Fig. 23 Vertical stiffness of a 200/60 R17 tire at 1.8 bar: experimental (black) and nonlinear model (gray)
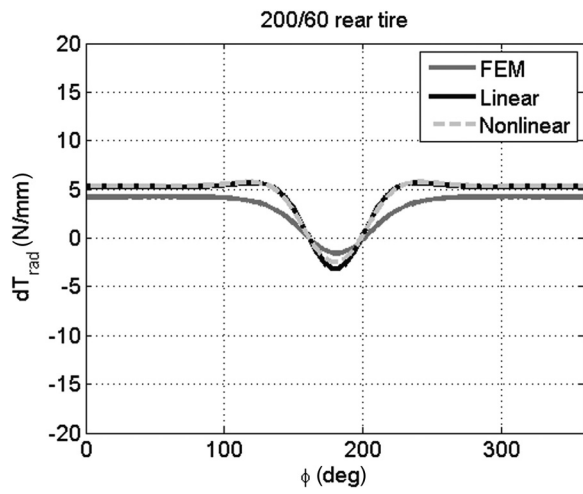


Fig. 24 Comparison of the radial forces acting on the wheel rim: 200/70 R17 rear tire, inflation pressure 1.8 bar, and vertical load 2950 N

The wheel is loaded with a uniform inflation pressure acting on the outer rim. The tire is replaced by the equivalent distribution of the radial and axial forces acting at the tire–rim interface. The distribution of the radial and axial forces acting at the tire–rim interface is computed by four different methods, namely, analytical
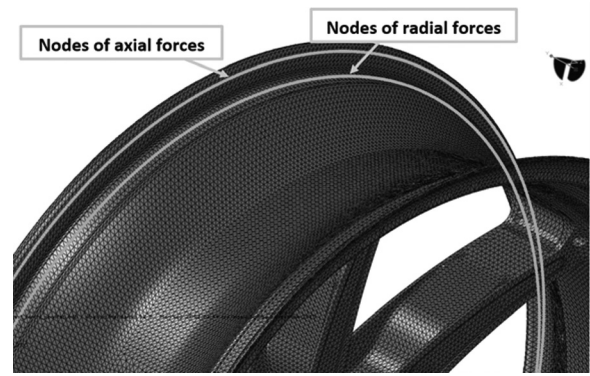


Fig. 26 Node sets for applying radial and axial reactions

reactions, FEM reactions, cosine loading function, and complete FEM. The analytical reactions and the FEM reactions methods are described in Secs. 2 and 3, respectively. The other two methods are briefly described in the following subsections (6.1 and 6.2). The radial and axial distributed forces are introduced as nodal forces. The radial forces are applied at the bead seats, while the axial forces are applied at the middle of the contact surface between the rim and tire sidewalls as shown in Fig. 26.

**6.1 Cosine Loading Function.** This is the most widely used loading method by wheels manufacturers. The effect of the tire is approximated by a cosine pressure distribution acting at the bead seats [1,4,5]. From the radial stiffness of the tire, the footprint length is estimated, and a cosine-distribution pressure is applied on an arch of 60 deg on the bead seats. The axial forces per unit length acting at the tire/rim interface are applied on the whole rim flange as shown in Fig. 27. The distributed force $T_f$ reads

$$T_f = \frac{p}{4r_f}\left(a^2 - r_f^2\right) \tag{32}$$

with $p$ as the inflation pressure, $a$ as the tire radius, and $r_f$ as the radius of the wheel rim.

**6.2 Complete Tire FE Model.** The physical models of the tire (Sec. 3) and the wheel rim are considered (Fig. 28). A frictional contact ($\mu = 0.5$ [30]) at the tire/rim interface is modeled. The tire is discretized with linear brick elements of average size of 6 mm. At the tire/rim contact surfaces, a finer mesh is employed. The vertical load is applied to a rigid plane that simulates the road surface as shown in Fig. 28.
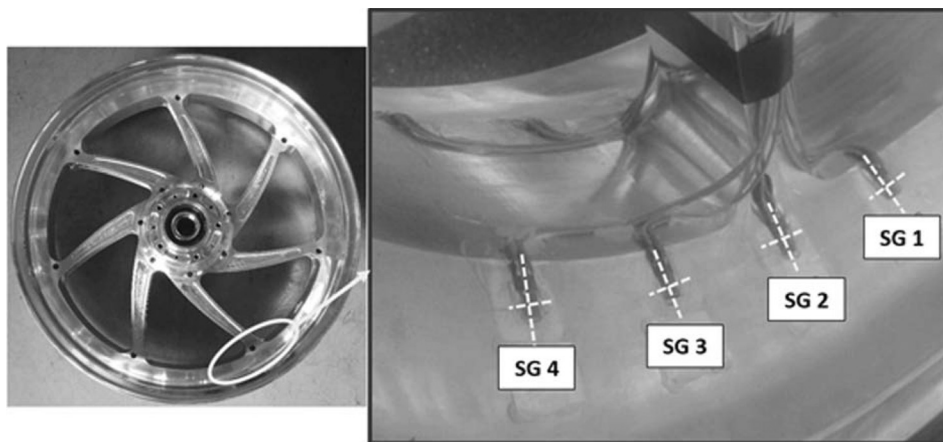


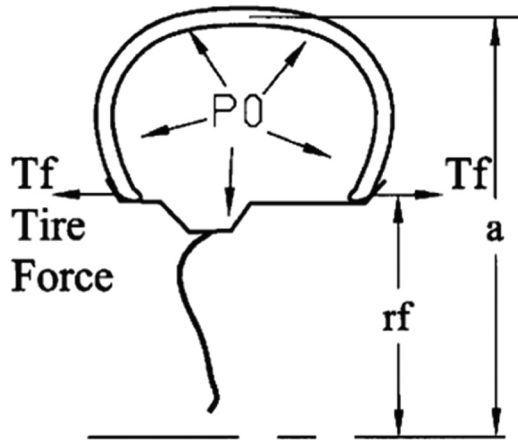Fig. 25 Location of the SG applied on the wheel rim

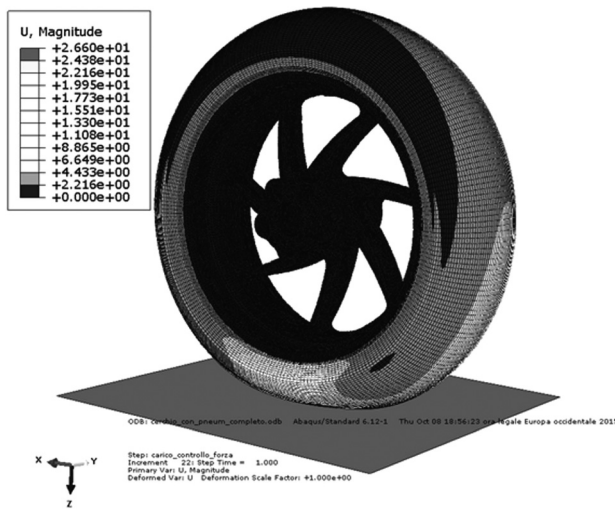**Fig. 27 Scheme of axial forces acting on the wheel rim—adapted from Ref. [5]**



**Fig. 28 Complete FE model of the tire and wheel rim subjected to a vertical load**

**6.3 Results.** Strain levels at the SG locations are computed for all the considered models and compared with the measured values. The comparison is reported in Table 6.

The results show that the cosine loading function tends to significantly overestimate the strain levels on the rim. The estimated deformation is more than double of the measured values with a difference of about 132% for the maximum measured deformation. Such an overestimation could be too conservative when high performance and lightweight wheels are designed. The analytical tire model provides more accurate results, with a difference with the maximum measured deformation of about 48%. Such difference is reduced to about 18% by using the FE model of the tire or

the full FE model. The full FE model provides the closest results for the two most stressed SG (SG2 and SG3).

## 7 Conclusions

In this paper, the computation of the reaction forces on a wheel rim was dealt with. The analytical and the FEM models of the race motorcycle tires were presented in this paper. The analytical model consists of a flexible ring on a suspended foundation. The ring accounts for the bending stiffness of the tread, while the elastic foundation describes the tire residual stiffness. The model computes reaction forces acting at the rim interface when the wheel is subjected to a radial distributed load.

The developed FEM model, on the other hand, accounts for the actual structure of the tire. Steel beads, 0 and 90 deg plies have been modeled. Incompressible Neo-Hooke constitutive relation is employed for describing the behavior of the rubber material.

The stiffness curves of the actual tires were obtained by means of experimental tests and were compared with the simulated ones. Both the analytical and FEM model showed a good agreement with the experimental results.

The reactions acting on the wheel at the tire–rim interface were computed from the analytical and the numerical models. The accuracy of the analytical model is quite good, especially if the simplicity of the model is taken into account.

Significant improvements in the analytical model were obtained by introducing a residual stiffness that depends on the tire deflection. In this case, a nonlinear differential equation was obtained and solved by means of finite difference method. The computed forces acting on the wheel rim are now closer to the FEM values, suggesting that geometric variations in the tire cross section due to the vertical deflection affect the local stiffness of the tire.

Finally, a comparison between the deformation measured by SG on a motorcycle wheel rim under a vertical load and the deformations computed by considering the tire/rim interface forces computed by different approaches was shown. The presented analytical model showed a consistent improvement in the accuracy with respect to the commonly employed approach of considering a cosine force distribution over a given rim angle with an error reduction of more than 60% for the most strained strain gauge. The FEM models of the tire showed a better accuracy, but at the cost of the knowledge of a larger set of parameters and of substantially larger computational times.

Despite its simplicity, the analytical model proved to be effective in describing the actual interaction between the tire and rim and could provide useful information on the way in which radial loads should be distributed on the wheel.

**Table 6 Comparison of the measured and simulated strains at the SG locations—strains are expressed in $\mu$m/m**

| Strain gauge | Measured | Complete model | Reactions from FEM | Reactions from analytical model | Cosine loading function |
|---|---|---|---|---|---|
| SG1 | −85 | −137 | −125 | −164 | −336 |
| SG2 | −250 | −287 | −295 | −370 | −580 |
| SG3 | −100 | −103 | −95 | −116 | −275 |
| SG4 | −60 | −79 | −58 | −50 | −143 |

## References

[1] Stearns, J., Srivatsan, T., Gao, X., and Lam, P., 2006, "Understanding the Influence of Pressure and Radial Loads on Stress and Displacement Response of a Rotating Body: The Automobile Wheel," Int. J. Rotating Mach., **2006**, p. 60193.

[2] Das, S., 2014, "Design and Weight Optimization of Aluminum Alloy Wheel," Int. J. Sci. Res. Publ., **4**(6).

[3] Wang, L., Chen, Y., Wang, C., and Wang, Q., 2011, "Fatigue Life Analysis of Aluminium Wheels by Simulation of Rotary Fatigue Test," J. Mech. Eng., **57**(1), pp. 31–39.

[4] Raju, P. R., Satyanarayana, B., Ramji, K., and Babu, K. S., 2007, "Evaluation of Fatigue Life of Aluminium Alloy Wheels Under Radial Loads," Eng. Failure Anal., **14**(5), pp. 791–800.

[5] Stearns, J., Srivatsan, T., Prakash, A., and Lam, P., 2004, "Modeling the Mechanical Response of an Aluminium Alloy Automotive Rim," Mater. Sci. Eng., **A366**, pp. 262–268.

[6] Lot, R., 2004, "A Motorcycle Tire Model for Dynamic Simulations," Meccanica, **39**(3), pp. 207–220.

[7] Cossalter, V., Doria, A., Lot, R., Ruffo, N., and Salvador, M., 2003, "Dynamic Properties of Motorcycle and Scooter Tires: Measurement and Comparison," Veh. Syst. Dyn., **39**(5), pp. 329–352.

[8] Lu, C., and Shih, M., 2005, "An Experimental Study on the Longitudinal and Lateral Adhesive Coefficients Between the Tyre and the Road for a Light Motorcycle," Veh. Syst. Dyn., **43**, pp. 168–178.

[9] Pauwelussen, J., Gootjes, L., Schröder, C., Köhne, K.-U., Jansen, S., and Schmeitz, A., 2003, "Full Vehicle ABS Braking Using the Swift Rigid Ring Tyre Model," Control Eng. Pract., **11**(2), pp. 199–207.

[10] Jansen, S., Zegelaar, P., and Pacejka, H., 1999, "The Influence of In-Plane Tyre Dynamics on ABS Braking of a Quarter Vehicle Model," Veh. Syst. Dyn., **32**(2–3), pp. 249–261.

[11] Mastinu, G., and Fainello, M., 1992, "Study of the Pneumatic Tyre Behaviour on Dry and Rigid Road by Finite Element Method," Veh. Syst. Dyn., **21**(1), pp. 143–165.

[12] Pacejka, H. B., 1972, "Analysis of the Dynamic Response of a Rolling String-Type Tire Model to Lateral Wheel-Plane Vibrations," Veh. Syst. Dyn., **1**(1), pp. 37–66.

[13] Clover, C., and Bernard, J. E., 1998, "Longitudinal Tire Dynamics," Veh. Syst. Dyn., **29**(4), pp. 231–260.

[14] Kim, S., Nikravesh, P., and Gim, G., 2008, "A Two-Dimensional Tire Model on Uneven Roads for Vehicle Dynamic Simulation," Veh. Syst. Dyn., **46**(10), pp. 913–930.

[15] Kindt, P., Sas, P., and Desmet, W., 2009, "Development and Validation of a Three-Dimensional Ring-Based Structural Tyre Model," J. Sound Vib., **326**(3–5), pp. 852–869.

[16] Kung, L., Soedel, W., and Yang, T., 1986, "Free Vibration of a Pneumatic Tire-Wheel Unit Using a Ring on an Elastic Foundation and a Finite Element Model," J. Sound Vib., **107**(2), pp. 181–194.

[17] Pinnington, R. J., and Briscoe, A. R., 2002, "A Wave Model for a Pneumatic Tyre Belt," J. Sound Vib., **253**(5), pp. 941–959.

[18] Pinnington, R. J., 2002, "Radial Force Transmission to the Hub From an Unloaded Stationary Tyre," J. Sound Vib., **253**(5), pp. 961–983.

[19] Larsson, K., and Kropp, W., 2002, "A High-Frequency Three-Dimensional Tyre Model Based on Two Coupled Elastic Layers," J. Sound Vib., **253**(4), pp. 889–908.

[20] Mastini, G., Gaiazzi, S., Montanaro, F., and Pirola, D., 1997, "A Semi-Analytical Tyre Model for Steady and Transient-State Simulations," Veh. Syst. Dyn., **27**, pp. 2–21.

[21] Mastinu, G., Previati, G., and Gobbi, M., 2011, "Analytical Computation of the Radial Stiffness of Pneumatic Tyres," 22nd IAVSD Symposium on Dynamics of Vehicles on Roads and Tracks, Manchester, UK.

[22] Hall, W., Mottram, J., and Jones, R., 2004, "Tire Modeling Methodology With the Explicit Finite Element Code LS-DYNA," Tire Sci. Technol., TSTCA, **32**(4), pp. 236–261.

[23] Meschke, G., Prayer, H., and Mang, H., 1997, "3D Simulations of Automobile Tires, Mesh Generation and Solution Strategies: Material Modeling," Tire Sci. Technol., TSTCA, **25**(3), pp. 154–176.

[24] Yang, X., 2011, "Finite Element Analysis and Experimental Investigation of Tyre Characteristics for Developing Strain-Based Intelligent Tyre Systems," Ph.D. dissertation, University of Birmingham, Edgbaston, UK.

[25] Yan, X., 2001, "Non-Linear Three-Dimensional Finite Element Modeling of Radial Tires," Math. Comput. Simul., **58**(1), pp. 51–70.

[26] Tönük, E., and Ünlüsoy, Y., 2001, "Prediction of Automobile Tire Cornering Force Characteristics by Finite Element Modeling and Analysis," Comput. Struct., **79**(13), pp. 1219–1232.

[27] Korunović, N., Trajanović, M., and Stojković, M., 2007, "FEA Tires Subjected to Static Loading," J. Serb. Soc. Comput. Mech., **1**, pp. 87–98.

[28] Ghoreisky, M., 2006, "Finite Element Analysis of the Steel-Belted Radial Tyre With Tread Pattern Under Contact Load," Iran. Polym. J., **15**, pp. 667–674.

[29] Korunović, N., Trajanović, M., Stojković, M., Mišić, D., and Milovanović, J., 2011, "Finite Element Analysis of a Tire Steady Rolling on the Drum and Comparison With Experiment," J. Mech. Eng., **57**(12), pp. 888–897.

[30] Pelle, R. G., 1994, "FEM Simulation of the Tire/Rim Seating Process," Tire Sci. Technol., **22**(2), pp. 76–98.

[31] Faria, L. O., Oden, J. T., Yavari, B., Tworzydlo, W. W., Bass, J. M., and Becker, E. B., 1992, "Tire Modeling by Finite Elements," Tire Sci. Technol., **20**(1), pp. 33–56.

[32] Jeusette, J. P., and Theves, M., 1992, "Finite Element Analysis of Tire/Rim Interface Forces Under Braking and Cornering Loads," Tire Sci. Technol., **20**(2), pp. 83–105.

[33] Lee, C., 2006, "Rim Slip and Bead Fitment of Tires: Analysis and Design," Tire Sci. Technol., **34**(1), pp. 38–63.

[34] Ballo, F., Gobbi, M., Mastinu, G., Previati, G., and Zerboni, R., 2015, "Motorcycle Tire Modeling," ASME Paper No. DETC2015-46607.

[35] Holzapfel, G., 2000, *Nonlinear Solid Mechanics: A Continuum Approach for Engineering*, Wiley, Hoboken, NJ.

[36] Alkan, V., Karamihas, S. M., and Anlas, G., 2011, "Finite Element Modeling of Static Tire Enveloping Characteristics," Int. J. Automot. Technol., **12**(4), pp. 529–535.

[37] Lei, L., Zuo, S., Yang, X., Wu, X., and Li, Y., 2010, "Finite Element Analysis of Radial Tires Based on the Software of MARC," 3rd International Conference on Advanced Computer Theory and Engineering (ICACTE), Vol. 1.

[38] Previati, G., and Kaliske, M., 2012, "Crack Propagation in Pneumatic Tires: Continuum Mechanics and Fracture Mechanics Approaches," Int. J. Fatigue, **37**, pp. 69–78.

[39] Simulia, 2012, *Abaqus 6.12 Analysis User's Manual 28.1.5*, Dassault Systèmes Simulia Corp., Providence, RI.

[40] Mastinu, G., Gobbi, M., and Previati, G., 2011, "A New Six-Axis Load Cell—Part I: Design," Exp. Mech., **51**(3), pp. 373–388.

[41] Gobbi, M., Previati, G., Guarnieri, P., and Mastinu, G., 2011, "A New Six-Axis Load Cell—Part II: Error Analysis, Construction and Experimental Assessment of Performances," Exp. Mech., **51**(3), pp. 389–399.

[42] Ballo, F., Gobbi, M., Mastinu, G., and Previati, G., 2014, "Advances in Force and Moments Measurements by an Innovative Six-Axis Load Cell," Exp. Mech., **54**(4), pp. 571–592.